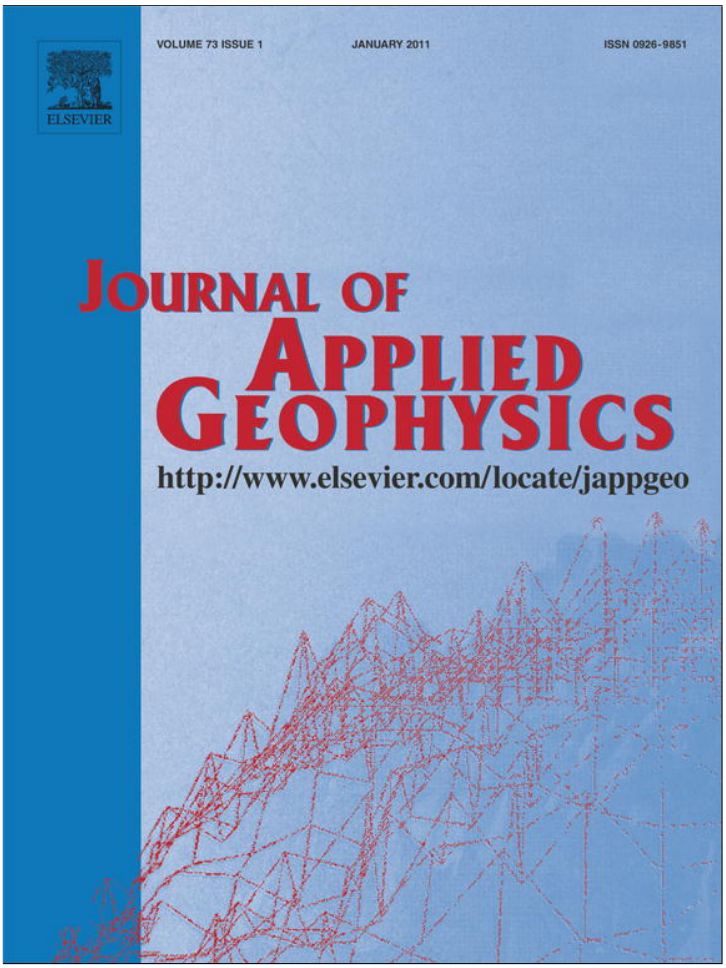

(This is a sample cover image for this issue. The actual cover is not yet available at this time.)

Journal of Applied Geophysics 74 (2011) 123–130

Contents lists available at ScienceDirect

Journal of Applied Geophysics

journal homepage: www.elsevier.com/locate/jappgeo

GPR-signal improvement using a Synthetic Emitter Array

Lorena Cedrina [a,b], Néstor Bonomo [a,b,*], Ana Osella [a,b]

[a] Departamento de Física, Facultad de Ciencias Exactas y Naturales, Universidad de Buenos Aires, Ciudad Universitaria, Pabellón 1, (1428) Buenos Aires, Argentina
[b] CONICET, Consejo Nacional de Investigaciones Científicas y Técnicas, Argentina

ARTICLE INFO

Article history:
Received 20 November 2009
Accepted 3 May 2011
Available online xxxx

Keywords:
GPR
Synthetic Emitter Array method
Signal to noise improvement
Lateral continuity improvement

ABSTRACT

We discuss improvements produced by a Synthetic Emitter Array on typical GPR reflection signals. We analyze their time and amplitude fluctuations and their intensity levels with respect to the surrounding signals. We compare the results of the method to those of the more usual Common Midpoint method, as well as the Single Offset results. We analyze diffractions at small objects and reflections at large interfaces for both simulated and real data. We evaluate the effects of different fluctuation levels in the soil parameters and the setting of the relative phases between the array components.

1. Introduction

Single transmitting and receiving antennae are used in most of the Ground-Penetrating Radar (GPR) applications. Usually, the distance between the antennae is kept constant (Single Offset (SO) surveys), and the antennae pair is moved along parallel lines, which cover the area of study. With this methodology, large portions of soil can be prospected in relatively short times and quality maps of the buried structures often result (Arts et al., 2009; Bavusi et al., 2009; Leucci and Negri, 2006; Shaaban et al., 2008). The acquisition of dense grids of parallel lines can provide detailed maps of targets (Francese et al., 2009; Hugenschmidt and Kalogeropoulos, 2009; Pérez-Gracia et al., 2009). SO methodologies have been applied to archeological prospection, pipe and tank detection, land-mine detection, engineering-structure characterization, forensic investigation, groundwater and leakage monitoring and shallow-geomorphology mapping, etc. (Bhosle et al., 2007; Bonomo et al., 2009; Fiedler et al., 2009; Gomez et al., 2009; Orlando and Slob, 2009; Pettinelli et al., 2008; Porsani and Sauck, 2007; Zyada et al., 2011). In this paper we discuss the use of a synthetic antennae array to improve GPR signals.

Different multi-offset methods have been used with GPR (Berard and Maillol, 2007; Lutz and Perroud, 2006; Nakashima et al., 2001; Pipan et al., 1999), the Common Midpoint (CMP) method being most usual. In CMP acquisition, single transmitting and receiving antennae are symmetrically moved on the surface from a midpoint, thus multiply sampling the ground below. Then, the data are averaged, which improves signal to clutter ratio with respect to the SO case. This procedure is commonly applied to a small number of midpoints to obtain the propagation velocity and depths of the main layers below them, below a few lines or, occasionally, below parallel lines to obtain both velocity and ground structure. With the CMP method the primary signals are reinforced in relation to random noise and clutter, improving the penetration and lateral coherence of the GPR signals. As occurs with other multi-offset methods, the most important limiting factor is the long time needed to acquire and process data.

The Emitter Array (EA) method is another multi-offset method that has been lately applied to GPR data to improve reflected signals (Cedrina et al., 2009; Lutz and Perroud, 2006). In this method a number of transmitting antennae (which constitute the emitter array) and a single component receiver are initially placed on the air–soil interface (Fig. 1). The number of antennae in the array and their relative distances and amplitudes are set in order to focus the transmitted fields (Cedrina et al., 2009), while the relative phases between the array components are selected to transmit the resulting beam toward the position estimated for the target and back to the receiver. When the transmitters-receiver group is moved along the investigated area, the relative positions of the antennae and target vary, so the relative phases between the array components are changed in order to redirect the energy along desired transmitters–reflector–receiver paths (Fig. 1). With this method, the lateral coherence of the primary signal and the amplitude ratio between the primary signal and the surrounding noise can be improved because clutter is reduced from unilluminated regions of soil and random events are averaged (Cedrina et al., 2009).

Concentration of the transmitted energy on a target can be obtained either by using a real set of closely spaced transmitting antennae, or with a single transmitter that is consecutively placed at the positions where the real array components would be, and then by superposing the fields of the individual records. This variant is called the Synthetic Emitter Array (SEA) method. Although EA and SEA methods are not physically equivalent, they lead to similar results. The SEA method is advantageous in that it overcomes signal differences

* Corresponding author. Tel.: +54 11 4576 3353; fax: +54 11 4576 3357.
E-mail address: bonomo@df.uba.ar (N. Bonomo).

0926-9851/$ – see front matter © 2011 Elsevier B.V. All rights reserved.
doi:10.1016/j.jappgeo.2011.05.001

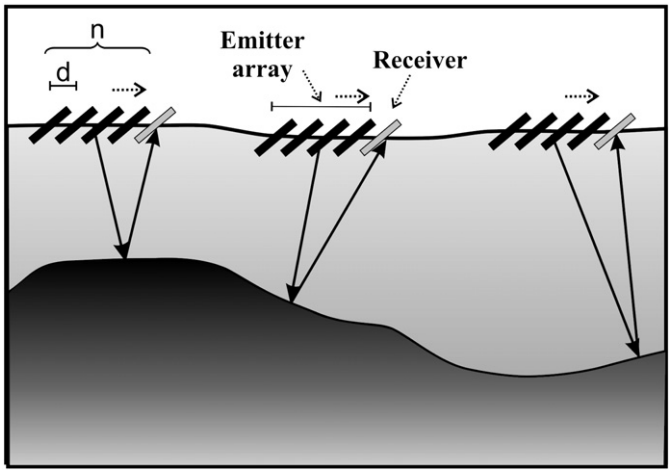

Fig. 1. Scheme of an emitter array and a receiver, both of which are moved along the survey line. We indicated with *n* the number of components in the array and with *d* the relative distances between them. The orientations of the antennae, which are perpendicular to the survey line, are also indicated.

and coupling between the transmitting elements, and requires simpler data acquisition and processing.

Synthetizing emitting fields is a well-known methodology in the seismic area (e.g. Shan and Biondi, 2008, Stoffa et al., 2006) and in the use of land, airborne and satellite radars (e.g. Thirion-Lefevre and Colin-Koeniguer, 2007; Wang, 2007). Nevertheless, very few applications have been carried out in GPR (Cedrina et al., 2009, Lutz and Perroud, 2006). In this case, near-field conditions are usual and far-field approximations cannot be normally applied.

In previous work, Lutz and Perroud (2006) showed that GPR SO signals from approximately flat horizontal reflectors can be improved through the SEA method. They analyzed how to increase the directivity of a synthetic emitting array located in a uniform space by varying the number of the array components, and their relative distances and phases. Later, we studied which characteristics of the transmitted wave-fronts are necessary to obtain satisfactory results in a half-space (Cedrina et al., 2009). We analyzed the dependence of the wave fronts on the parameters of the array and the distance from the center of the array to the target, for near-field to far-field conditions. We showed a methodology that worked not only with extended reflectors but also with small-size diffractors. The SEA method was useful to make visible very weak and apparently discontinuous signals, which couldn't be defined through the SO method.

Although the signal improvements obtained through the SEA method were qualitatively evident from previous work, it is also necessary a quantitative analysis of these improvements to ascertain their main characteristics with precision. In this article we evaluate the signal improvements produced by the SEA method and compare the SEA results to those of the most common GPR methods. In particular, we look at lateral fluctuations of the main reflections and their amplitude levels with respect to the surrounding. We analyze two basic situations: the diffraction at a small object and the reflection at a flat interface. In particular, we consider the effects produced by different fluctuation levels in the soil matrix, and the importance of the relative phase setting. We analyze simulated and real data.

2. Numerical simulations

The fields transmitted by synthetic emitter arrays depend on the characteristics of the transmitter, the number and relative orientations, positions, amplitudes and phases of the components in the array, and the constitutive and geometrical characteristics of the soil interfaces. Aligned dipole-type transmitters polarized orthogonally to the survey line are often used in the SEA method to transmit and receive the fields (Fig. 1). For this kind of configuration, analysis of simulated fields (Cedrina et al. 2009) showed that the resulting beam has a minimum width for a relatively small number of dipoles *n*, for typical distances *d* between the dipoles and distances to the targets. The initial decrement in the width vs. *n* curve is a consequence of a decrement in the beam divergence, while the subsequent increment simply occurs because of the increasing size of the array with respect to the distance from the array to the target, since both lengths are comparable. Furthermore, the array wave-front significantly differs from a single-transmitter wave-front for raising *n*, which results in complex or uninterpretable reflections. This occurs because the wave-path lengths from each array component to the evaluation point compare with the main wavelengths of the field and increasingly differ among them, so the resultant wave-form becomes complicated. These characteristics indicate that it is necessary to adequately select *n* to effectively concentrate the energy on the target and maximize the effects of the average, and at the same time to maintain the single transmitter waveform at the target position.

Cedrina et al. (2009) also found that the wave-fronts are more complex for larger *d* (keeping constant *n* and the other parameters), which is also a consequence of increasingly different individual wave-path lengths. Although smaller values of *d* produce more adequate wave-fronts for the application of the SEA method, this parameter is usually limited in practice by the attainable precision of the antennae positions.

Once *n* and *d* have been established, the relative phase determined by the time shift $\Delta\tau$ between the emitted wavelets, is selected at each position on the ground in order to direct the transmitted beam along adequate transmitter–reflector–array paths (Fig. 1). Below, we evaluate the effects of this parameter on the results of the SEA method, particularly on the fluctuation and amplitude levels of the resulting signal. In parallel, we analyze the influence of the soil matrix on the SEA results. Spatial fluctuations in the soil parameters can produce secondary diffractions that interfere with the signal of interest, so it is important to analyze to what extent the SEA method improves the continuity and amplitude level of this signal.

To simulate the fields we use a 2D finite-differences code (Irving and Knight, 2006), for the TE mode. Although the radiation patterns and geometrical spreading of realistic dipole-type GPR antennas cannot be properly modeled with this 2D code (since a fully 3D approach should be necessary) we can obtain the main relevant features of the fields by applying it.

2.1. Small diffractor profiles

The first model we analyze is shown in Fig. 2a. A sphere with a diameter 5 cm is located at a depth 80 cm. The object has a relative permittivity $\varepsilon_r = 5.25$ and a conductivity $\sigma = 2.5$ mS/m. The surrounding half-space medium has $\varepsilon_r = 3.5$ and $\sigma = 1$ mS/m. The medium above is air. The grid interval is 1 cm in both directions. Random spatial fluctuations for every grid element, with maximum amplitude 20%, are applied to the soil parameters. All the dipoles are located at the air–soil interface, centered at the *x*-axis (the direction of the survey), with dipole-axes parallel to *y*. The central frequency of the emitted wavelet is $f_c = 500$ MHz (wavelength = 32 cm inside the soil) and the −3 dB bandwidth $\Delta f = 300$ MHz (full range ≈1 GHz).

In Fig. 2b, we show a SO profile obtained for the model in Fig. 2a. The offset in the figure is $\Delta x = 0.3$ m, whereas the *x*-coordinate refers to the midpoint between the transmitter and receiver positions. The reflection signal from the diffractor can be observed with difficulty in the figure, as a hyperbola with vertex at 11 ns, approximately, due to comparable intensities for the main and surrounding signals and interference.

Fig. 2c shows a result of the SEA-method for the model in Fig. 2a. The relative amplitudes and distances between the array components are $A = 1$ and $d = 0.1$ m, respectively. For these parameters, $n = 4$ is

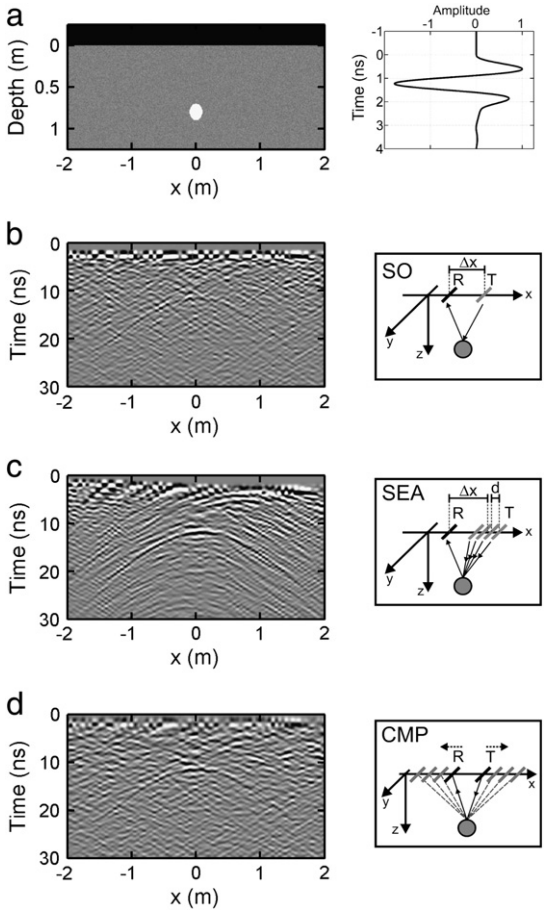

Fig. 2. a) Model of a small diffractor located at 80 cm depth. The transmitted pulse is shown at the right-hand side of the model. b) The SO profile obtained for this model. The offset for this figure is $\Delta x = 0.3$ m. c) The SEA result, for a number of array components $n = 4$, relative amplitudes $A = 1$, relative distances $d = 0.1$ m, equivalent offset $\Delta x = 0.3$ m, and time-shift interval $-06 < \Delta\tau < 0.6$ ns. d) The CMP result for a number of stacking $m = 4$.

the largest amount of dipoles for which the resulting wave front does not significantly distort at the target position. The *x*-coordinate refers here to the midpoint between the center of the array and the receiver position. The equivalent offset Δx, defined between these positions, is $\Delta x = 0.45$ m. We selected time shifts $-0.6\ \text{ns} \le \Delta\tau \le 0.6$ ns, which corresponds to transmission angles between 50° and −50°, to improve the signal of the diffractor at consecutive *x*-intervals. We used a total of 8 intervals to obtain the result in Fig. 2c.

When Fig. 2b and c are compared, it can be observed that the signal for the SEA method is more visible than the original SO signal. At this point, it is unclear if this improvement is mainly related to a lower fluctuation of the signal or an increased signal to clutter intensity ratio. With respect to this, not only the signal from the main diffractor has been reinforced in Fig. 2c but also parts of the signals from the surrounding diffractors (the fluctuations of the soil matrix). These can be observed in the figure as constant-slope fringes, parallel to the main signal, inside each *x*-interval. Then, the resulting signal to clutter ratio could be similar to the original. In addition, a number of signals perpendicular to the main signal appeared inside the outermost intervals (e.g., x = (−2–−1) m and x = (1–2) m), which are consequences of the onset of a small subsidiary lobe in the transmitted pattern for $|\Delta\tau| > 0.4$ ns, and could also affect the continuity and intensity of the SEA results.

In Fig. 2d, we show a result of the CMP method for the model in Fig. 2a. The number of stacking in the figure is $m = 4$. From a comparison of Fig. 2d and b it can be observed that the CMP diffraction for the model is clearer than the one for the SO case. On the other hand, the comparison of Fig. 2c and d shows a clearer signal for the SEA method than for the CMP method. This result is due to the attenuation of the signals from secondary reflectors outside the transmitted beam in the SEA method.

2.2. Small diffractor analysis

To quantitatively evaluate the results of the SO, SEA and CMP methods, we analyzed the time and amplitude fluctuations along the main reflections and their intensities with respect to the background intensities. To measure the time fluctuations, we calculated the time of maximum amplitude for the selected reflection in each trace, compared this time to the times of the adjacent traces, and normalized the result. This magnitude, which we called "normalized time difference" (NTD), was calculated for the diffraction signals in Fig. 2b to d as a function of *x*: the results are shown in Fig. 3a. A running average through 9 consecutive values in the curves was applied in order to smooth them. We used a dark line for the SEA result, a dark gray for the SO result and a light gray for the CMP result. Fig. 3a shows that the SEA method has reduced the NTD throughout the entire x-interval. Furthermore, the respective curve is less varying than the others and extends over a larger *x*-range. These characteristics are also related to a better visualization of the respective diffraction signal. Globally, the average values of NTD, calculated throughout the entire *x*-interval, are 0.60×10^{-2}, 1.61×10^{-2} and 1.64×10^{-2} for the SEA, SO and CMP methods, respectively, which indicates a significant improvement on the original NTD through the application of the SEA method.

To measure the amplitude fluctuations for the reflections of interest, we shifted the traces in time using the time of the maximum of the reflection and correlated the results of neighboring traces in a time interval centered at the reflection. We show the curves that result in Fig. 3b. Averages of 9 consecutive values were calculated along the curves to smooth them. The SEA method increased the correlation in approximately 95% of the x-range, yielding the least fluctuating curve. On the contrary, in the interval x = (0.25–0.45) m, the SEA curve is below the SO curve. This kind of anomalous behavior sometimes occurs in regions where a secondary signal crosses the main signal, due to an occasional distortion of the reflected wavelet. With respect to the CMP method, we observe that it has also improved the original correlation in different x-intervals, although its results are below the SEA ones. The global correlations for the three methods, calculated throughout the entire *x*-range, are indicated in Table 1.

In Fig. 3c we show quotients between the average intensities of the signal and surrounding clutter, for the SEA, SO and CMP methods. To obtain these curves, we averaged the intensity inside three 1.5-period time intervals defined along each trace. The first interval is centered at the main event to evaluate its mean intensity, whereas the other two are symmetrically disposed around the main event to evaluate the mean surrounding intensity. The resulting quantity has been defined "signal to noise intensity ratio" (STNIR). When the curves in Fig. 3c are compared, we find that the SEA method led to the highest values of STNIR in most of the curve (90%).

The first analyzed example showed that the improvement of the signal produced by the SEA method is related to a decrease in the fluctuations and an increase in the signal to noise intensity ratio. The magnitudes of the improvements on the NTD, correlation and STNIR curves vary with the position, and also their relative weights, with no appreciable correlation between the positions of the maxima in the curves. In general, when the fluctuations of the soil matrix decrease, the NTD curves smooth and approximate to the constant value 0 (curves not shown), whereas the overall relative improvement produced by the SEA method diminishes. For example, for a 20% fluctuation of the soil parameters, the overall SEA value divided by the overall SO value is 0.37, which is below the respective quotient of the

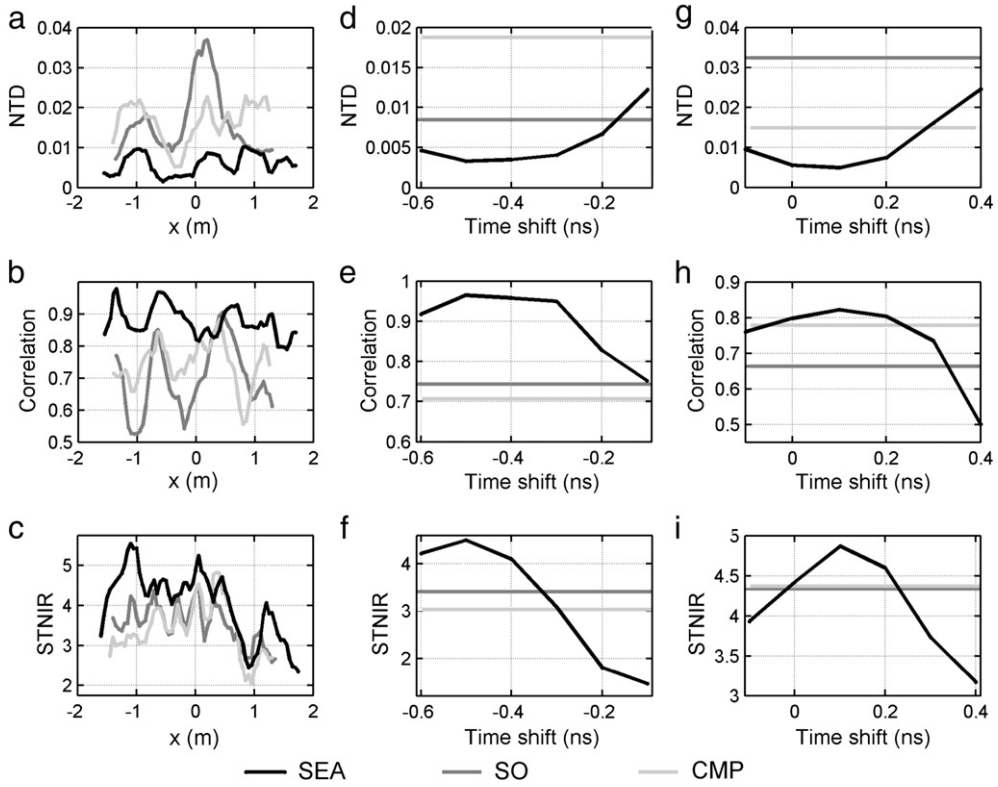

Fig. 3. a) The normalized time difference for the maxima of the diffraction signal in Fig. 2b to d, b) the correlation between adjacent traces, and c) the signal to noise intensity ratio, all of them as functions of the position along the survey line. d) The averaged NTD as a function of the time shift $\Delta\tau$. The interval of average is x = (−1.5–−1.1) m, at the extreme left of the diffraction signals. e) The average correlation, for the interval at the left extreme of the signal, f) the average STNIR, for the interval at the left extreme of the signal, g) the average NTD, for an interval at the center of the signal (x = (−0.2–0.2) m), h) the average correlation, for the interval at the center of the signal, and i) the average STNIR, for the interval at the center of the signal.

10% case, 0.46. Similarly, the relative overall NTD for the CMP method diminishes from 1.04 to 1.02.

The correlation curves also smooth and approximate to a constant value, in this case 1, with a lower relative improvement on the signal when the soil fluctuations are reduced. For a 20% fluctuation, the relative overall correlation for the SEA and CMP methods are 1.26 and 1.07, above the respective values of the 10% case of 1.09 and 0.98. On the contrary, the absolute and relative values of the STNIR increase when the fluctuation level diminishes, while the curves of the three methods become less fluctuant and overlapping. For a 20% fluctuation of the soil parameters, the overall relative STNIR for the SEA and CMP methods are 1.14 and 0.96, which are below the 10% values, 1.26 and 1.09, respectively.

We next analyze the effects of the selection of the transmitted-beam direction on the results of the SEA method. To do this, we define an x-interval and average the previous magnitudes inside it, for each $\Delta\tau$ (time shift). Fig. 3d shows the average NTD for the three methods. In this case, the average interval x = (−1.5–−1.1) m is located at the extreme left of the diffraction signals. It can be observed that the SEA curve presents a peak with a minimum at $\Delta\tau = -0.5$ ns. The $\Delta\tau$ values

Table 1
The NTD, the correlation and the STNIR, averaged through the entire x-range, for the synthetic and experimental examples. The fluctuation levels in the soil parameters are indicated in the synthetic examples. The last two columns refer to the relative values of these quantities.

			SEA	SO	CMP	SEA/SO	CMP/SO
Diffractor	NTD	Synthetic 20% fluct.	0.60×10^{-2}	1.61×10^{-2}	1.64×10^{-2}	0.37	1.02
		Synthetic 10% fluct.	0.31×10^{-2}	0.67×10^{-2}	0.70×10^{-2}	0.46	1.04
		Experimental	0.41×10^{-2}	1.19×10^{-2}	0.94×10^{-2}	0.34	0.79
	Correlation	Synthetic 20% fluct.	0.87	0.69	0.74	1.26	1.07
		Synthetic 10% fluct.	0.92	0.84	0.83	1.09	0.98
		Experimental	0.90	0.75	0.87	1.20	1.16
	MTSIR	Synthetic 20% fluct.	4.02	3.53	3.40	1.14	0.96
		Synthetic 10% fluct.	5.41	4.26	4.67	1.26	1.09
		Experimental	2.67	2.17	2.42	1.22	1.11
Horizontal reflector	NTD	Synthetic 20% fluct.	0.29×10^{-2}	1.25×10^{-2}	0.83×10^{-2}	0.22	0.66
		Synthetic 10% fluct.	0.19×10^{-2}	0.57×10^{-2}	0.31×10^{-2}	0.33	0.54
		Experimental	0.51×10^{-2}	0.62×10^{-2}	0.62×10^{-2}	0.82	1.01
	Correlation	Synthetic 20% fluct.	0.94	0.78	0.87	1.20	1.11
		Synthetic 10% fluct.	0.98	0.92	0.97	1.07	1.05
		Experimental	0.93	0.91	0.94	1.02	1.02
	MTSIR	Synthetic 20% fluct.	5.70	3.59	4.85	1.58	1.35
		Synthetic 10% fluct.	11.60	5.37	8.17	2.15	1.52
		Experimental	2.49	1.99	2.54	1.24	1.27

of the peak correspond to the transmission angles that better direct the energy along the transmitter–reflector–receiver path. The correlation and STNIR curves, Fig. 3e and f, also present peaks, with maxima at $\Delta\tau = -0.5$ ns. Note that these curves can be used to select a time shift that optimizes the SEA results, and that this selection is not so critical because of the considerable widths of the peaks. For example, the CMP method simultaneously improves the original NTD, correlation and STNIR from $\Delta\tau = -0.6$ ns to $\Delta\tau = -0.3$ ns, which is a wide interval.

Fig. 3g, h and i are analogous to Fig. 3d, e and f, respectively, but for an average interval centered at the origin ($x = (-0.2\text{–}0.2)$ m). The SEA curves present similar characteristics than the previous, except for the positions of their extremes, which are located at $\Delta\tau = -0.1$ ns. Also in this case the SEA method simultaneously improves these magnitudes in a wide interval, from $\Delta\tau = 0.0$ ns to $\Delta\tau = 0.2$ ns.

2.3. Linear reflector profiles

The second model we analyze is shown in Fig. 4a. It is a flat horizontal reflector located at 80 cm depth. The shallowest stratum is characterized by a relative permittivity $\varepsilon_r = 3.5$ and a conductivity $\sigma = 1$ mS/m, whereas the deepest stratum by $\varepsilon_r = 4$ and $\sigma = 2$ mS/m. The fluctuation level in the soil matrix is 20%. The other parameters, as the dipole configuration and wavelet characteristics are the same that those in the previous model.

In Fig. 4b, we show a SO profile ($\Delta x = 0.3$ m) obtained for the model in Fig. 4a. The reflection signal from the horizontal interface can be clearly observed at 11 ns, approximately. In Fig. 4c, we show the respective SEA result. As for the previous model, the array parameters are $A = 1$, $d = 0.1$ m and $n = 4$. In this case, we applied a constant time shift $\Delta\tau = 0.1$ ns (transmission angle $-10°$) for all x. From a comparison of Fig. 4b and c we see that the SEA method improved the SO signal. Also the CMP result, Fig. 4d, improved the original signal, although less than the SEA method.

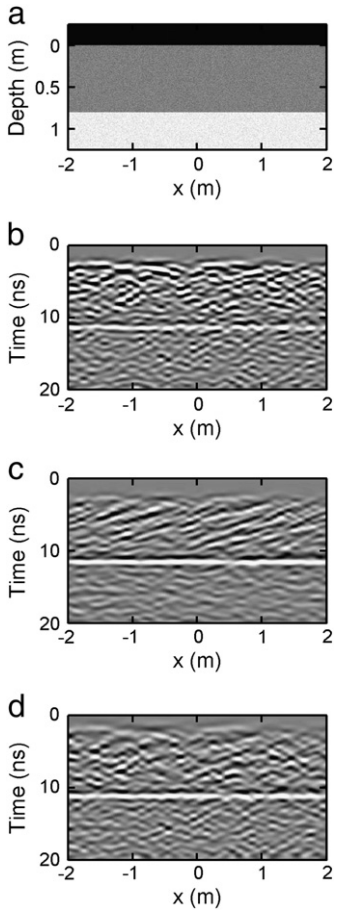

Fig. 4. a) Model of flat horizontal reflector located at 80 cm depth, b) the SO profile for this model ($\Delta x = 0.3$ m), c) the SEA profile ($n = 4$, $A = 1$, $d = 0.1$ m, $\Delta x = 0.3$ m, $\Delta\tau = 0.1$ ns), and d) the CMP profile ($m = 4$, $\Delta x = 0.3$ m). The array parameters for Fig. 4b to d are the same that for Fig. 2b to d, respectively.

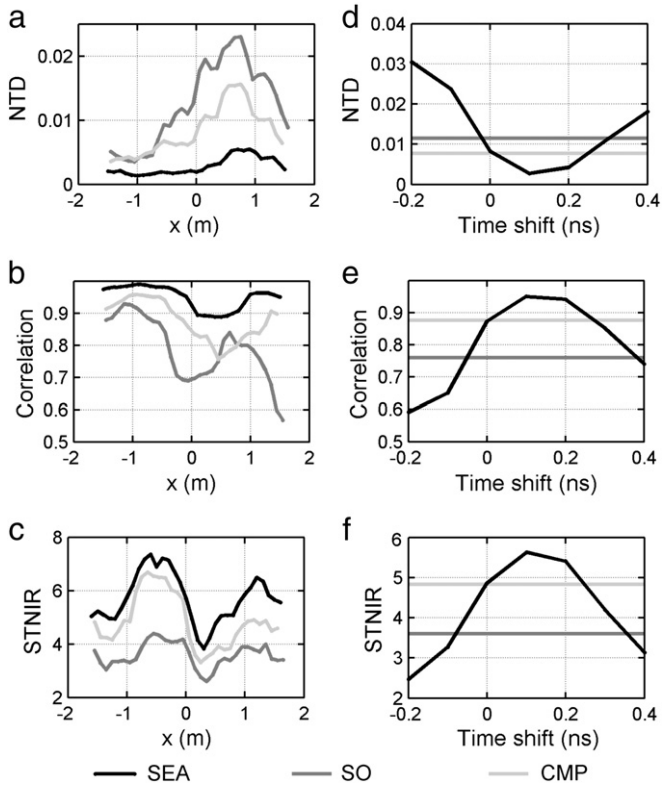

Fig. 5. a) The normalized time difference for the horizontal flat reflector in Fig. 4b) the correlation, and c) the STNIR, all of them as functions of the position along the survey line. d) The average NTD as a function of $\Delta\tau$, e) the average correlation, and f) the average STNIR.

2.4. Linear reflector analysis

To confirm these observations, in Fig. 5a to c we show the NTD, correlation and STNIR curves, respectively, for the SEA, SO and CMP signals. We obtained the curves through the same procedures used in the diffractor case. It can be observed that the SEA and CMP methods improved the SO results for the three magnitudes, with better results from the SEA method. In fact the overall (averaged through the entire x-interval) NTD, correlation and STNIR values, are 0.29×10^{-2}, 1.25×10^{-2} and 0.83×10^{-2} for the SEA, SO and CMP results, respectively.

As in the diffractor case, the improvement on the NTD and correlation curves obtained through the SEA and CMP methods for the horizontal reflection diminishes when the fluctuation level in the soil matrix is decreased (see Table 1 for the relative values of these magnitudes). On the contrary, the STNIR improvement increases when the soil fluctuations diminish.

In Fig. 5d, e and f we show the average NTD, correlation and STNIR values, as functions of $\Delta\tau$, for the flat horizontal reflector. In this case, the entire x-range had been used for the average. It can be observed that the SEA curves are qualitatively similar to the curves previously obtained for the diffractor (Fig. 3d to Fig. 3i), particularly to those calculated by averaging in an x-interval centered at the position of the object (Fig. 3g and i), since for these positions both situations are approximately similar.

3. Experimental example: diffractor

In previous work we showed (Cedrina et al., 2009) that the SEA method can be useful to make visible very weak and apparently discontinuous signals, apparently by increasing both the signal to noise ratio and the continuity of the event. Here we show two experimental examples to evaluate the signal level and continuity. We acquired the data using the experimental setup displayed in Fig. 6a. An approximately spherical object, with a maximum diameter of 20 cm was positioned at a depth of 110 cm and covered with the natural soil, mainly composed of dry sand and a lower proportion of clay. Both the transmitting and receiving antennae were located on the air–soil interface, along the x-axis, the direction of the survey, with antennae axes parallel to y. We used a Sensors & Software Pulse EKKO PRO radar system and 500 MHz antennae.

In Fig. 6b, we show a SO profile ($\Delta x = 0.25$ m) obtained along the ground section in Fig. 6a. The diffraction signal from the buried object can be clearly seen in the figure, with vertex at 10 ns. A number of additional diffraction hyperbolae and approximately-horizontal reflections, which are produced at the natural discontinuities of the soil, also appear in the figure. For example, an approximately-horizontal signal of a stratum can be observed around 8 ns, between about $x = 0.8$ m and $x = 2.4$ m. The left end of this signal continues in a diffraction signal (vertex at 0.8 m) originated at the point where the setup excavation cut the stratum.

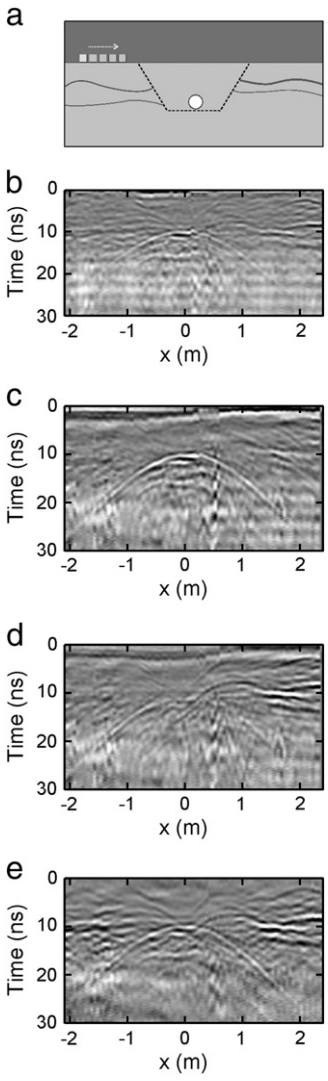

Fig. 6. a) Setup used to acquire the field data. The dotted lines indicate the limits of the preparatory excavation. b) The SO profile ($\Delta x = 0.25$ m), c) the SEA profile that improves the signal of the buried object ($n = 4$, $A = 1$, $d = 0.1$ m, $\Delta x = 0.3$ m, $-0.6 < \Delta\tau < 0.6$ ns), d) the SEA profile that improves the signal of the approximately horizontal reflector located at t ≈ 8 ns, 0.8 m < x < 2.4 m and the associated diffraction signal with vertex at (t, x) = (8 ns, 0.8 m) ($n = 4$, $A = 1$, $d = 0.1$ m, $\Delta x = 0.3$ m, $-0.5 < \Delta\tau < 0.2$ ns), and e) the CMP result ($m = 4$).

Fig. 6c shows the result of the SEA method for the diffraction at the buried object. The array parameters are $A = 1$, $d = 0.1$ m, $n = 4$ and $\Delta x = 0.1$ m, whereas we selected time shifts -0.6 ns $< \Delta\tau < 0.6$ ns (transmission angles between 50° and −50°) to improve this signal at consecutive x-intervals. A total of 7 intervals were used. In Fig. 6d, we selected a different set of time shifts, -0.5 ns $< \Delta\tau < 0.2$ ns (transmission angles 47° and −21°), in order to highlight the aforementioned approximately-horizontal reflection and associated hyperbola. On the other hand, Fig. 6e shows the CMP result for a number of stack $m = 4$.

When Fig. 6b to e are compared, we find that the SEA and CMP signals are clearer than the SO ones, with better results for the SEA signals. Moreover, the SEA method improved the signals from the buried object and the stratum in a selective form: the main diffraction signal is intensified (Fig. 6c), while the approximately horizontal signal and associated diffractions attenuated or, alternatively, the approximately horizontal signal and associated diffractions are intensified while the main diffraction signal attenuated (Fig. 6d).

We analyzed the fluctuations and relative amplitudes of the signals mentioned in Fig. 6b to e by calculating the NTD, correlation and STNIR. Fig. 7a, b and c show the results for the main diffraction signal. We see that the SEA method improved the SO results in most of the x-range (90%, 100% and 84% of the range, for the respective magnitudes). Also the CMP method improved the original curves, although less than the SEA method. The global values of NTD, correlation and STNIR improvements, calculated along the entire x-range, are indicated in Table 1. From the comparison of Fig. 3a to c and Fig. 7a to c we also find that the experimental and simulated examples behaved similarly throughout the curves.

In Fig. 7d, e and i, we show curves of the averaged NTD, correlation and STNIR as functions of $\Delta\tau$, for an average interval x = (−1.2–−0.8) m located at the left extreme of the diffraction signals. Fig. 7g, h and i shows similar curves, but for an average interval x = (−0.2–0.2) m located at the center of the signals. As in the simulated examples, the SEA curves show peaks for those values of $\Delta\tau$ that better direct the energy along the transmitter–reflector–receiver path. The $\Delta\tau$-interval in which the SEA method improves the SO results is greater than 0.2 ns, wide enough to make possible an easy selection of this parameter.

4. Experimental example: linear reflector

As a last example, we analyze the reflection at the approximately-horizontal stratum that was highlighted through the SEA method in Fig. 6b. Fig. 8a to c shows the NTD, correlation and STNIR curves, for the SEA, SO and CMP signals. It can be observed that both the SEA and CMP methods improved the SO curves in most of the x-range, including the interval related to the associated diffraction (x < 1 m). Because of the low fluctuation and amplitude levels in the original signal, the benefits of the SEA method are more moderate in this example than in the previous, with similar SEA and CMP results. Finally, in Fig. 8d to f, we show curves of the average NTD, correlation and STNIR, as functions of $\Delta\tau$, for an average interval x = (1.0–2.5) m, located in the approximately horizontal part of the signals. These curves confirm the characteristics observed in the previous examples.

5. Conclusions

We have analyzed the signal improvements produced by the Synthetic Emitter Array (SEA) method. We simulated the fields produced by

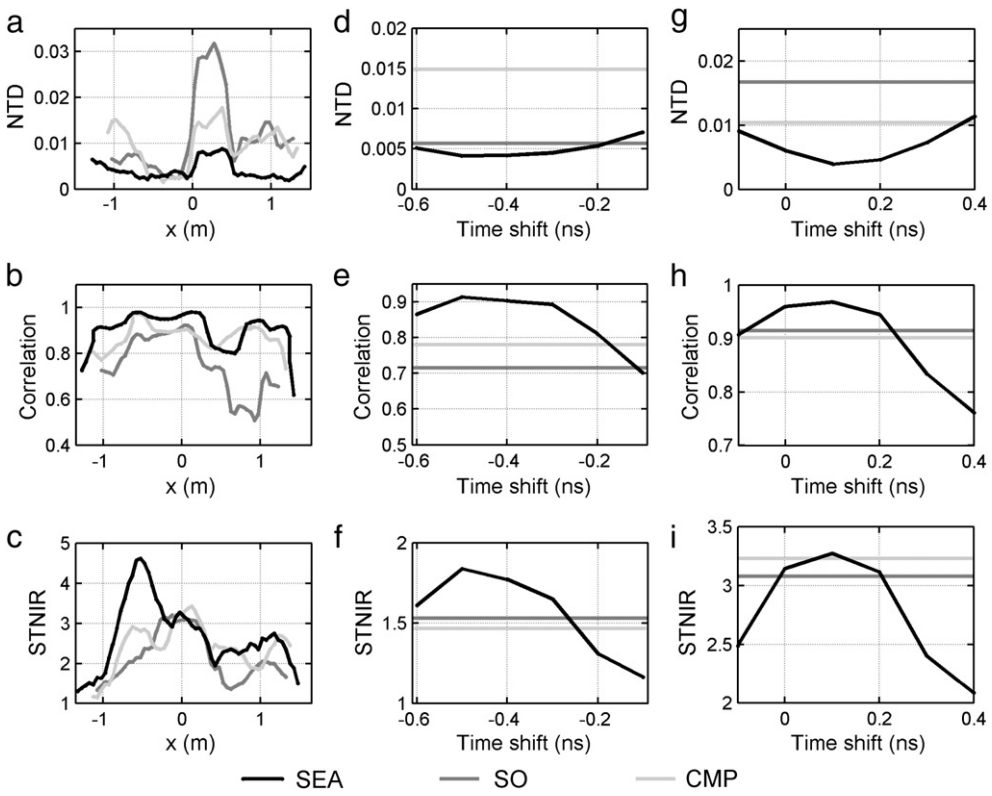

Fig. 7. a) The NTD for the diffraction signal from the buried object in the experimental example, b) the correlation between adjacent traces, and c) the STNIR, all of them as functions of the position along the survey line. d) The average NTD as a function of $\Delta\tau$. The interval for the average is x = (−1.2–−0.8) m, at the left extreme of the signals. e) The average correlation, for the interval at the left extreme of the signal, f) the average STNIR, for the interval at the left extreme of the signal, g) the average NTD, for an interval at the center of the signal (x = (−0.2–0.2) m), h) the average correlation, for the interval at the center of the signal, and i) the average STNIR, for the interval at the center of the signal.

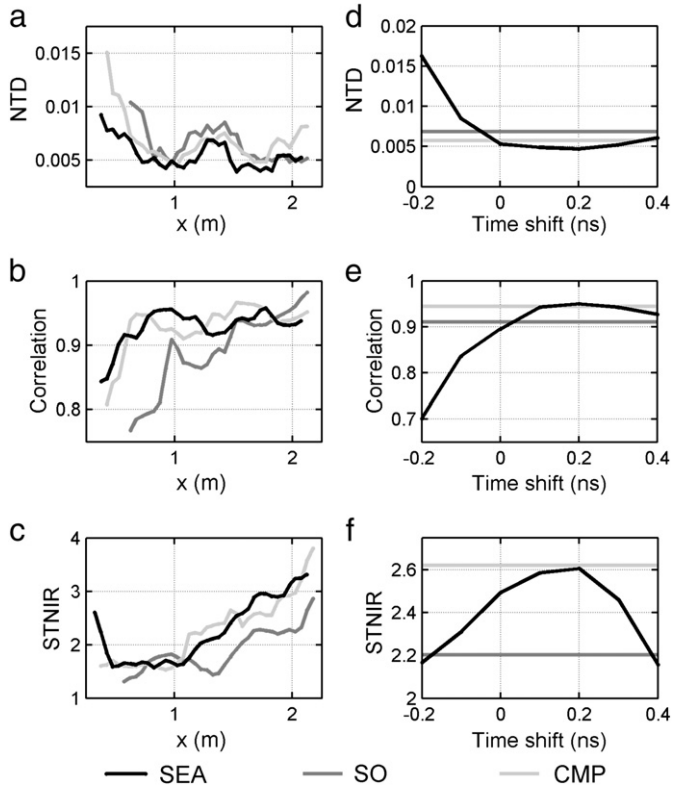

Fig. 8. a) The NTD for the approximately horizontal reflector in the experimental example, b) the correlation, and c) the STNIR, all of them as functions of the position along the survey line. d) The average NTD as a function of $\Delta\tau$, e) the average correlation, and f) the average STNIR.

dipole-type arrays and considered two basic situations: the diffraction at a small object and the reflection at a flat interface.

The signals obtained through the SEA method became clearer than the Single Offset (SO) and CMP signals, as a consequence of the efficient attenuation of secondary signals from reflectors outside the propagating beams. The improvements simultaneously occurred with a decrease of the fluctuations in time and amplitude and an increase in the signal to noise intensity ratio. The relative importances of these variables changed with the position of the antennae along the survey, without a noticeable correlation between the NTD, correlation and STNIR curves. In general, the SEA curves varied with position less than the others, which is another characteristic related to a better visualization of the signals. Furthermore, the SEA curves could be calculated over larger x-ranges for the diffraction signals, due to improvements obtained towards the extremes of these hyperbolae.

The effects of the transmitted-beam direction (time shift) on the results of the SEA method showed that the SEA signals presented peaks for time shifts that more efficiently directed energy along the transmitter–reflector–receiver paths. For these peaks, the results of the SEA method exceeded the SO results for time-shift intervals with considerable widths. Therefore the selection of this parameter is not critical during the SEA method implementation.

The simulated and experimental curves were qualitatively similar. The simulated examples showed that the improvements in the time and amplitude fluctuations diminished when the fluctuation level in the soil matrix decreased, and that the improvement in the signal to noise intensity ratio increased when the soil fluctuations diminished. The experimental examples also illustrated the ability of the SEA method to selectively improve nearby GPR signals of different objects.

The benefits of the SEA method to improve desired signals from diffractors and strata are clear from this and previous work (Cedrina et al., 2009). The method is particularly useful to reduce the time and

amplitude fluctuations of weak signals and, to a less extent, their intensity with respect to the background. It can be used, for example, to make very weak reflections or diffractions visible, to visualize apparently discontinuous strata and to define the borders of reflecting surfaces, etc. Then, it can be a good complement of the habitual SO surveys. More specifically, it can be used after a SO survey, around the positions where marginal signals occurred. Moreover, the method can be applied in parallel to or after other multi-offset methods without acquiring additional data. In particular, the SEA method can be used to analyze a selected group of signals after a CMP analysis, without too large efforts.

In the SEA method, the continuity and amplitude level of the signal are improved because clutter is reduced from unilluminated regions of soil and random events are averaged. Using array components with non-uniform relative distances, phases and amplitudes could be a possible way to optimize the focusing of energy on the target, thus further improving the SEA results. Using 2D arrays, with array components positioned along and at the sides of the survey line could improve focalization in the perpendicular direction, also improving the final results.

Acknowledgments

This work was partially supported by grants from CONICET (Consejo Nacional de Investigaciones Científicas y Técnicas) and ANPCyT (Agencia Nacional de Promoción Científica y Tecnológica).

References

Arts, R., Baradello, L., Girard, J., Kirby, G., Lombardi, S., Williamson, P., Zaja, A., 2009. Results of geophysical monitoring over a “leaking” natural analogue site in Italy. Energy Procedia 1, 2269–2276.

Bavusi, M., Giocoli, A., Rizzo, E., Lapenna, V., 2009. Geophysical characterisation of Carlo's V Castle (Crotone, Italy). Journal of Applied Geophysics 67, 386–401.

Berard, B., Maillol, J., 2007. Multi-offset ground penetrating radar data for improved imaging in areas of lateral complexity — application at a Native American site. Journal of Applied Geophysics 62, 167–177.

Bhosle, B., Parkash, B., Awasthi, A., Singh, V., Singh, S., 2007. Remote sensing-GIS and GPR studies of two active faults, Western Gangetic Plains, India. Journal of Applied Geophysics 61, 155–164.

Bonomo, N., Cedrina, L., Osella, A., Ratto, N., 2009. GPR prospecting in a prehispanic village, NW Argentina. Journal of Applied Geophysics 67, 80–87.

Cedrina, L., Bonomo, N., Osella, A., 2009. Application of the Synthetic Emitter-Array method to improve GPR signals. Journal of Applied Geophysics revised version submitted on July 7, 2009.

Fiedler, S., Illich, B., Berger, J., Graw, M., 2009. The effectiveness of ground-penetrating radar surveys in the location of unmarked burial sites in modern cemeteries. Journal of Applied Geophysics 68, 380–385.

Francese, R., Finzi, E., Morelli, G., 2009. 3-D high-resolution multi-channel radar investigation of a Roman village in Northern Italy. Journal of Applied Geophysics 67, 44–51.

Gomez, C., Lavigne, F., Hadmoko, D., Lespinasse, N., Wassmer, P., 2009. Block-and-ash flow deposition: a conceptual model from a GPR survey on pyroclastic-flow deposits at Merapi Volcano, Indonesia. Geomorphology 110, 118–127.

Hugenschmidt, J., Kalogeropoulos, A., 2009. The inspection of retaining walls using GPR. Journal of Applied Geophysics 67, 335–344.

Irving, J., Knight, R., 2006. Numerical modeling of ground-penetrating radar in 2-D using MATLAB. Computers & Geosciences 32, 1247–1258.

Leucci, G., Negri, S., 2006. Use of ground penetrating radar to map subsurface archaeological features in an urban area. Journal of Archaeological Science 33, 502–512.

Lutz, P., Perroud, H., 2006. Phased-array transmitters for GPR surveys. Journal of Geophysics and Engineering 3, 35–42.

Nakashima, Y., Zhou, H., Sato, M., 2001. Estimation of groundwater level by GPR in an area with multiple ambiguous reflections. Journal of Applied Geophysics 47, 241–249.

Orlando, L., Slob, E., 2009. Using multicomponent GPR to monitor cracks in a historical building. Journal of Applied Geophysics 67, 327–334.

Pérez-Gracia, V., Caselles, J., Clapes, J., Osorio, R., Martínez, G., Canas, J., 2009. Integrated near-surface geophysical survey of the Cathedral of Mallorca. Journal of Archaeological Science 7, 1289–1299.

Pettinelli, E., Beaubien, S., Lombardi, S., Annan, P., 2008. GPR, TDR, and geochemistry measurements above an active gas vent to study near-surface gas-migration pathways. Geophysics 73, A11–A15.

Pipan, M., Baradello, L., Forte, E., Prizzon, A., Finetti, I., 1999. 2-D and 3-D processing and interpretation of multi-fold ground penetrating radar data: a case history from an archaeological site. Journal of Applied Geophysics 41, 271–292.

Porsani, J., Sauck, W., 2007. Ground-penetrating radar profiles over multiple steel tanks: artifact removal through effective data processing. Geophysics 72, J77–J83.

Shaaban, F., Abbas, A., Atya, M., Hafez, M., 2008. Ground-penetrating radar exploration for ancient monuments at the Valley of Mummies—Kilo 6, Bahariya Oasis, Egypt. Journal of Applied Geophysics 68, 194–202.

Shan, G., Biondi, B., 2008. Plane-wave migration in tilted coordinates. Geophysics 73, S185–S194.

Stoffa, P., Sen, M., Seifoullaev, R., Pestana, R., Fokkema, J., 2006. Plane-wave depth migration. Geophysics 71, S261–S272.

Thirion-Lefevre, L., Colin-Koeniguer, E., 2007. Investigating attenuation, scattering phase center and total height using simulated interferometric SAR images of forested areas. IEEE Transactions on Geosciences and Remote Sensing 45, 3172–3179.

Wang, W., 2007. Approach of adaptive synchronization for bistatic SAR real-time imaging. IEEE Transactions on Geosciences and Remote Sensing 45, 2695–2700.

Zyada, Z., Matsuno, T., Hasegawa, Y., Sato, S., Fukuda, T., 2011. Advances in GPR-based landmine automatic detection. Journal of the Franklin Institute 348, 66–78.